



## A constitutive model for the in-plane mechanical behavior of nonwoven fabrics

Alvaro Ridruejo<sup>a</sup>, Carlos González<sup>a,b</sup>, Javier Llorca<sup>a,b,\*</sup>

<sup>a</sup>Department of Materials Science, Polytechnic University of Madrid and CISDEM, E.T.S. de Ingenieros de Caminos, 28040 Madrid, Spain

<sup>b</sup>Madrid Institute for Advanced Studies of Materials, IMDEA Materials Institute, C/Profesor Aranguren s/n, 28040 Madrid, Spain

### ARTICLE INFO

#### Article history:

Received 19 November 2011

Received in revised form 20 March 2012

Available online 3 May 2012

#### Keywords:

Constitutive modeling

Nonwoven fabrics

Deformation

Damage

### ABSTRACT

A constitutive model is presented for the in-plane mechanical behavior of nonwoven fabrics. The model is developed within the context of the finite element method and provides the constitutive response for a mesodomain of the fabric corresponding to the area associated to a finite element. The model is built upon the ensemble of three blocks, namely fabric, fibers and damage. The continuum tensorial formulation of the fabric response rigorously takes into account the effect of fiber rotation for large strains and includes the nonlinear fiber behavior. In addition, the various damage mechanisms experimentally observed (bond and fiber fracture, interfiber friction and fiber pull-out) are included in a phenomenological way and the random nature of these materials is also taken into account by means of a Monte Carlo lottery to determine the damage thresholds. The model results are validated with recent experimental results on the tensile response of smooth and notched specimens of a polypropylene nonwoven fabric.

© 2012 Elsevier Ltd. All rights reserved.

### 1. Introduction

Nonwoven fabrics are structural materials manufactured from a set of disordered fibers consolidated by bonds of different nature (simple entanglement, local thermal fusion, chemical binders, etc.). They are becoming more popular in many engineering applications (ballistic protection, thermal insulation, liquid-absorbing textiles, fireproof layers, geotextiles, etc.) due to the lower processing costs and improved properties (energy absorption), as compared to woven counterparts. Moreover, new nonwoven materials have emerged recently as a consequence of the advent of fibers with reduced manipulability, such as nanotube sheets (Berhan et al., 2004a,b; Berhan and Sastry, 2007) or nanofiber felts directly produced by electrospinning (Dzenis, 2004).

Further optimization of the mechanical behavior of these materials requires a better understanding of the relationship between microstructure and mechanical behavior which can only be achieved through the development of physically-based constitutive models. In addition to this, models are also necessary to predict the mechanical performance of structural elements. Modeling a nonwoven fabric may be considered a daunting task not only because of the randomness of the microstructure (very different from the regular one found in woven or knitted textiles), but also because of its particularly complex response, which often includes large deformations and rotations, bond and fiber fracture,

fiber sliding and a continuous rearrangement of the fiber network topology.

The first attempt to model a nonwoven fabric was made by Cox (1952). In this seminal work, aimed at studying the mechanical behavior of paper, he considered a random network of long, elastic, noninteracting fibers and was able to calculate its elastic constants within a small-deformation framework. Cox's contribution was extended by Kallmes and Corte (1960), who introduced the areal density of bonds and free fiber length using a geometrical probabilistic theory. Most of the models following this line assume a shear-lag transfer of load between fibers, which has proved successful for predicting the tensile behavior of paper (Carlsson and Lindstrom, 2005). This approach is no longer accurate, however, when the load is transferred through axial stresses at the fiber intersections (Räsänen et al., 1997).

Backer and Petterson (1960) addressed the problem of the tensile deformation of purely nonwoven assemblies by means of a linear elastic orthotropic model. Since simple orthotropic models do not contain microstructural information, they were not able to reproduce the effect of the microstructure's evolution – in particular, fiber reorientation – and were therefore restricted to the small strain regime. In order to enrich the fabric mechanics and take into account the nonuniform fiber orientation, Bais-Singh and Goswami (1995) and Liao et al. (1997) modeled the nonwoven fabric as a stack of planar laminae, each of them containing fibers oriented along one single direction. This way, they were able to predict the effect of fiber orientation for small deformations although the bonding between layers overconstrains the fiber rotation (allowed only if the entire lamina rotates). In addition, Liao and Adanur (1999) implemented a fiber failure criterion which rendered good

\* Corresponding author at: Department of Materials Science, Polytechnic University of Madrid and CISDEM, E.T.S. de Ingenieros de Caminos, 28040 Madrid, Spain. Tel.: +34 91 549 34 22; fax: +34 91 550 30 47.

E-mail addresses: [javier.llorca@upm.es](mailto:javier.llorca@upm.es), [javier.llorca@imdea.org](mailto:javier.llorca@imdea.org) (J. Llorca).

agreement with the experimental results of two polyester fabrics up to 20% strain.

Another class of model takes into account the actual microstructure by explicitly including the fiber network structure of the fabric. Computationally costly though they are, they allow a more realistic approximation of the micromechanisms involved during deformation. This computational cost usually precludes three-dimensional descriptions and limits the analyses to the in-plane response, with the notable exception of the model by Termonia (2003), whose aim was to study the bending of nonwoven layers. These models can essentially be divided into two sets. In the first one, fibers are considered to be the fundamental constituents of the nonwoven fabric and bonds are regarded as “indestructible” (Britton et al., 1983, 1984b,a; Wu and Dzenis, 2005), whereas the second group is focused on the bond motion and evolution (Grindstaff and Hansen, 1986; Jirsak and Lukas, 1991; Jirsak et al., 1993). More recently, Ridruejo et al. (2010) simulated the behavior of a glass–fiber nonwoven fabric through a finite element simulation of the network in which the fiber yarns were explicitly represented. Following the experimental observations, fiber yarns did not fail and bonds were responsible for the load transmission and the eventual fabric failure. The role of friction between fiber yarns after bond fracture was introduced through a stick–slip law. Comparison with experiments provided very accurate results in smooth and notched samples loaded in tension.

The problem of computational cost can be addressed by obtaining the fabric properties using homogenization techniques over a representative volume instead of the whole fabric. This approach was first applied to nonwovens by Petterson (1959), who considered a set of straight fibers in a unit cell oriented according to a certain statistical distribution and linked by rigid bonds. The overall deformation imposed on the fabric was accommodated by the fibers in each unit cell following an affine transformation and the angular integration of the fiber stress contributions provided the stress normal to an arbitrary plane. This “fiber web model” included the post-yield properties of the fibers and a weakest-link treatment of the unit cell fracture. It was modified by Hearle and Stevenson (1964), who introduced the effect of fiber curling, and by Kothari and Patel (2001), who considered a time-dependent fiber response, while Narter et al. (1999) extended the model to 3D. Finally, other authors (Diani et al., 2004; Bischoff et al., 2002; Gasser et al., 2006) developed constitutive models for nonwoven fabrics assuming a particular fiber distribution within the representative volume element. The macroscopic response was derived through a hyperelastic formulation where the strain energy density function is obtained by adding the contributions from each fiber. More recently Silberstein et al. (2012) have also developed an elastic–plastic micromechanical model based on a multilayer triangulated network. Within a slightly different frame, Planas et al. (2007) presented a macroscopic model for fiber-reinforced materials with deformable matrices based on the equivalence between the virtual works of the fiber-reinforced and the equivalent continuum media. These models based on homogenization have been very useful for modeling and understanding the complex behavior of nonwoven fabrics but they present two important limitations: they can neither take into account the changes in the network topology due to damage nor include the localization of damage (a common problem associated with all homogenization schemes).

In this paper, a new constitutive model is presented for the in-plane mechanical response of nonwoven fabrics. The model is developed within the context of the finite element method and provides the constitutive response for a mesodomain of the fabric corresponding to the area associated to a finite element. Thus, the computational cost is reasonable because it is not necessary to represent each fiber of the network but the localization of damage in the fabric can be accounted for. The behavior of the fibers in the

mesodomain basically starts with Petterson’s assumptions (Petterson, 1959) by considering a set of noninteracting straight fibers with an arbitrary initial orientation. The effect of fiber rotation for large strains and the nonlinear fiber behavior are rigorously taken into account by the continuum tensorial formulation. In addition, the various damage mechanisms experimentally observed (bond and fiber fracture, fiber friction and pull-out) are included in the model in a phenomenological way and the random nature of these materials, as well as the changes in fiber connectivity, are also included by means of a Monte Carlo lottery to determine the damage thresholds. The model results are validated against recent experimental results on the tensile response of smooth and notched specimens of a polypropylene nonwoven fabric (Ridruejo et al., 2011).

## 2. Experimental background

The constitutive model developed in this paper is based on a detailed experimental characterization of the deformation and failure micromechanisms of a polypropylene nonwoven felt (Ridruejo et al., 2011). The main results are briefly recalled here for the sake of completion, as they stand for the model’s physical foundations. The nonwoven fabric analyzed was a geotextile made of polypropylene fibers of 40–60  $\mu\text{m}$  in diameter. The continuous spun fibers were then laid down randomly on a flat surface producing an isotropic fiber web sheet which was then bonded by the simultaneous application of pressure and heat, leading to partial fusion between fibers at the entanglement points. The fabric areal density was  $\rho = 118 \pm 2 \text{ g/m}^2$ .

Individual fibers were extracted from the felts by carefully pulling with tweezers and tested in tension. The engineering stress – engineering strain curves ( $s_f - e_f$ ) were bilinear, the elastic region being characterized by the elastic modulus  $E_f$  and the inelastic region by the hardening modulus  $H_f$ . Their values as well as those of the engineering yield strength,  $s_f^y$ , the engineering tensile strength,  $s_f^u$ , and the strain-to-failure,  $e_f^u$  are shown in Table 1, which presents the average values and the standard deviations corresponding to 15 tests.

Uniaxial tensile tests of fabric rectangular specimens of 200 mm width and 100 mm height were carried out under stroke control at a cross-head speed of 0.8 mm/s. After a short linear region, the curves presented marked nonlinear behavior and the maximum load carrying capacity was attained at engineering strains of the order of 30–40%. Afterwards, the gradual reduction of the stress borne by the fabric was interrupted by one (or, sometimes, two) abrupt reductions in stress, associated with the sudden localization of damage. The curves presented a long tail as the stresses carried by the fabric were reduced to zero at engineering strains above 100%. The deformation pattern at different stages during deformation is shown in Fig. 1.

Another set of tests was carried out on coupons of the same dimensions with central notches whose length was equal to 20%, 40%, and 60% of the specimen width. It was found that the polypropylene nonwoven fabric was notch insensitive and the shape of the stress–strain curve was equivalent to the one observed in the unnotched coupons regardless of the initial notch size: the maximum in the load-carrying capacity was attained after significant nonlinear deformation and the samples presented an abrupt reduc-

**Table 1**

Density and parameters of the engineering stress–engineering strain curve of polypropylene fibers extracted from the nonwoven fabric.

$\rho_f$ (g/cm <sup>3</sup> )	$E_f$ (GPa)	$s_f^y$ (MPa)	$H_f$ (MPa)	$s_f^u$ (MPa)	$e_f^u$
0.91	1.7 $\pm$ 0.1	120 $\pm$ 4	59 $\pm$ 2	240 $\pm$ 10	1.4 $\pm$ 0.1

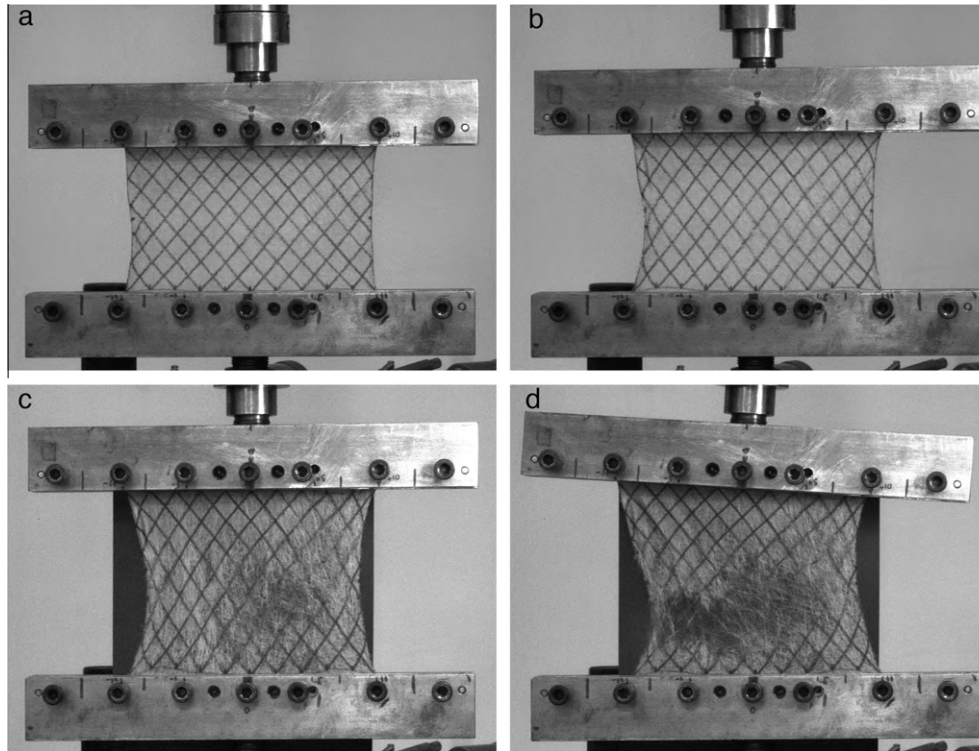


**Fig. 1.** Deformation pattern of the rectangular specimen subjected to tensile deformation. (a) Far-field strain of 15% (77% of the maximum load). (b) Far-field strain of 25% (94% of the maximum load). (c) Far-field strain of 46.5% (94% of the maximum load, after the peak). (d) Far-field strain of 47%, corresponding to the instant after localization of fracture (32% of the maximum load).

tion in strength after the peak load, followed by a long tail. The deformation pattern of a notched coupon is shown in Fig. 2. The large nonlinear deformation capability led to a complete blunting of the crack, reducing the stress concentration at the tips. Load was channeled through the ligaments in front of both notch tips, without any noticeable difference in the mechanisms with respect to the unnotched specimens.

The dominant deformation and damage phenomena at the microscopic scale were ascertained by means of mechanical tests inside an scanning electron microscope (Ridruejo et al., 2011). It was found that damage began at very low strains by fracture of interfiber bonds, which caused rearrangement of the fiber orientation and reduction in the fabric stiffness. This process (bond breakage and fiber reorientation) continued upon loading, leading to a marked nonlinearity in the stress–strain curve behavior. The maximum load was attained under these conditions without any evidence of fiber fracture although fibers oriented in the loading direction underwent plastic deformation. Further bond breakage resulted in the localization of damage within the fabric, leading to the development of a fracture zone of sparse fabric mainly made up of fibers aligned in the loading direction. These mechanisms were responsible for the considerable deformability and energy-absorption capability of the fabric, which also presented excellent strength and was notch-insensitive.

### 3. Constitutive model for the nonwoven fabric

The objective of this section is to develop a constitutive model for the in-plane deformation of nonwoven fabrics which is able to explicitly take into account the main deformation and failure micromechanisms experimentally observed. Thus, the model should account for the extensive fiber rotation, the elastic–plastic deformation of the polypropylene fibers and progressive damage due to interbond fracture, which leads to the localization of

fracture and to the re-arrangement of the fiber network. In order to attain this goal, the model is made up of three blocks built on top of each other: the network model, the fiber model and the damage model. These are described below.

#### 3.1. Fiber network model

The structure and deformation of the fiber network is taken into account through a continuum model developed by Planas et al. (2007), which constitutes a finite strain extension of the pioneering work by Cox (1952). The model considers a square planar region of arbitrary size containing a random network of long, straight, non-interacting fibers. Each fiber is characterized by a unit vector  $\mathbf{N}$  (Fig. 3), which forms an angle  $\Theta$  with respect to a privileged direction (e.g. the loading axis). This square planar region is considered unloaded and is taken as our reference configuration.

If the square region is subjected to a certain imposed deformation, given by the deformation gradient tensor  $\mathbf{F}$ , each fiber will deform according to its orientation. The fiber stretch,  $\lambda_f$ , is expressed as

$$\lambda_f = \frac{l}{l_0} = \sqrt{\mathbf{C} \cdot \mathbf{N} \cdot \mathbf{N}} \quad (1)$$

where  $l$  and  $l_0$  stand for the fiber length in the actual and reference configuration, respectively, and  $\mathbf{C} = \mathbf{F}^T \mathbf{F}$  is the right Cauchy–Green strain tensor. Furthermore, the engineering stress  $s_f$  carried by the fibers will be a function of the fiber stretch as

$$s_f = \frac{T}{\Omega_0} = s_f(\lambda_f) \quad (2)$$

where  $T$  is the longitudinal traction applied on the fiber and  $\Omega_0$  the initial fiber cross section. The mechanical power per unit volume of fiber associated to the force  $T$  acting on the fiber is expressed as:

$$\dot{\omega} = \frac{T \dot{l}}{\Omega l} = \frac{T \dot{\lambda}_f}{\Omega \lambda_f} \quad (3)$$

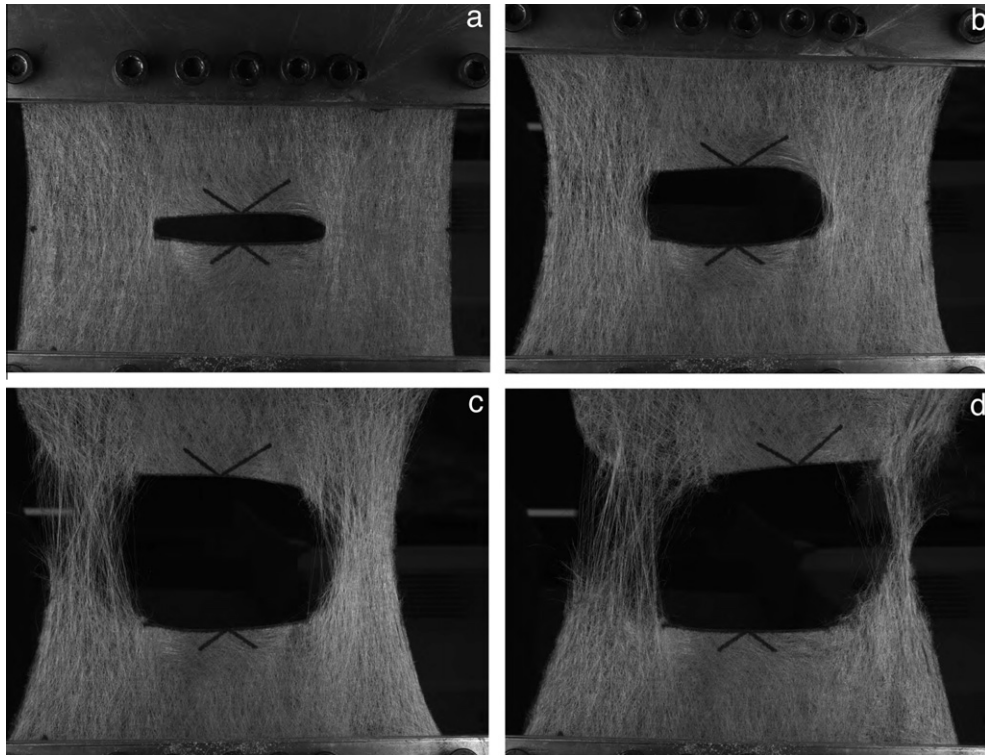


**Fig. 2.** Deformation pattern of the rectangular specimen with a central notch of 40% of the width subjected to tensile deformation. (a) Far-field strain of 10% (70% of the maximum load). (b) Far-field strain of 33% (maximum load). (c) Far-field strain of 67% (70% of the maximum load, after the peak). (d) Far-field strain of 70%, corresponding to the instant after localization of fracture (10% of the maximum load).

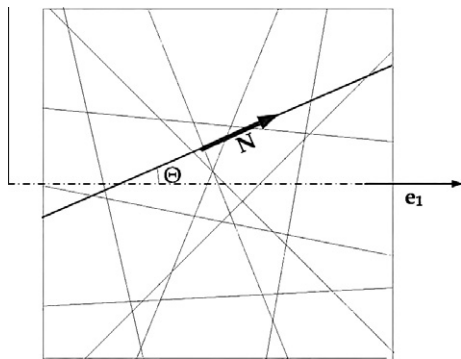


**Fig. 3.** Fiber network in the reference configuration.

where  $\Omega$  stands for the current fiber cross section. Assuming that fiber deformation takes place without volume change ( $\Omega l = \Omega_0 l_0$ ) and using Eq. (1), the mechanical power per unit volume of fiber,  $\dot{\omega}$  can be written in the reference configuration as

$$\dot{\omega} = s_f(\lambda_f) \dot{\lambda}_f = s_f(\lambda_f) \frac{\dot{\mathbf{C}}\mathbf{N} \cdot \mathbf{N}}{2\sqrt{\mathbf{C}\mathbf{N} \cdot \mathbf{N}}} \quad (4)$$

Re-arranging terms following the rules of tensorial algebra, it follows

$$\dot{\omega} = \text{tr} \left[ s_f(\lambda_f) \frac{(\mathbf{N} \otimes \mathbf{N})\dot{\mathbf{C}}}{2\sqrt{\mathbf{C}\mathbf{N} \cdot \mathbf{N}}} \right] \quad (5)$$

The extension of this expression to a fiber network can be carried out easily by taking into account that the fabric is made up of sets of fibers with different orientation. If  $\Psi(\theta)$  is the fraction of fibers forming an angle  $\theta$  (determined by  $\mathbf{N}^\theta$ ) with the reference

direction, the mechanical power per unit volume of fibers in the fabric,  $\dot{\omega}^{fabric}$ , is given by

$$\dot{\omega}^{fabric} = \text{tr} \left[ \sum_{\theta} f_f^\theta s_f^\theta(\lambda_f) \Psi(\theta) \frac{(\mathbf{N}^\theta \otimes \mathbf{N}^\theta)}{2\sqrt{\mathbf{C}\mathbf{N}^\theta \cdot \mathbf{N}^\theta}} \dot{\mathbf{C}} \right], \quad (6)$$

where  $f_f$  is the volume fraction of the fibers.

Let us now consider a homogeneous solid, subjected to an arbitrary deformation given by  $\mathbf{C}$ . The mechanical power per unit volume due to deformation can be written in the reference configuration in terms of the second Piola–Kirchhoff stress tensor as:

$$\dot{\omega} = \text{tr} \left[ \frac{1}{2} \dot{\mathbf{S}}\dot{\mathbf{C}} \right] \quad (7)$$

and this homogeneous solid will be equivalent to the fabric in terms of the mechanical power stored or dissipated by the system if

$$\text{tr} \left[ \frac{1}{2} \dot{\mathbf{S}}\dot{\mathbf{C}} \right] \equiv \text{tr} \left[ \sum_{\theta} f_f^\theta s_f^\theta(\lambda_f) \Psi(\theta) \frac{(\mathbf{N}^\theta \otimes \mathbf{N}^\theta)}{2\sqrt{\mathbf{C}\mathbf{N}^\theta \cdot \mathbf{N}^\theta}} \dot{\mathbf{C}} \right] \quad (8)$$

for all possible arbitrary deformations given by  $\dot{\mathbf{C}}$ . This equivalence is valid irrespectively of the conservative or nonconservative nature of the forces. Thus, the constitutive behavior of the nonwoven fabric can be expressed in terms of the second Piola–Kirchhoff stress tensor as

$$\mathbf{S} = \sum_{\theta} f_f^\theta s_f^\theta(\lambda_f) \Psi(\theta) \frac{(\mathbf{N}^\theta \otimes \mathbf{N}^\theta)}{\sqrt{\mathbf{C}\mathbf{N}^\theta \cdot \mathbf{N}^\theta}} \quad (9)$$

where the information concerning fiber orientation should be also provided in the reference configuration because the second Piola–Kirchhoff stress tensor considers forces and areas in the reference

configuration. In a more general case, the fiber orientation is given by the planar orientation distribution function  $\Psi(\Theta)$ , defined as the probability for a fiber to be oriented in the interval  $(\Theta, \Theta + d\Theta)$ . Obviously,

$$1 = \int_{-\frac{\pi}{2}}^{\frac{\pi}{2}} \Psi(\Theta) d\Theta \quad (10)$$

and  $\Psi(\Theta) = 1/\pi$  in the case of an isotropic fabric. Therefore the constitutive equation of the fabric can be expressed as

$$\mathbf{S} = s_f \int_{-\frac{\pi}{2}}^{\frac{\pi}{2}} s_f^\theta(\lambda_f) \Psi(\Theta) \frac{(\mathbf{N}^\theta \otimes \mathbf{N}^\theta)}{\sqrt{\mathbf{CN}^\theta \cdot \mathbf{N}^\theta}} d\Theta \quad (11)$$

and the Cauchy stress tensor in the current (deformed) configuration is given by

$$\boldsymbol{\sigma} = \frac{1}{J} \mathbf{FSF}^T \quad (12)$$

where  $J$ , the Jacobian, is the determinant of  $\mathbf{F}$ .

Another important outcome of the model is the degree of orientation of the fibers within the fabric, characterized by the orientation index  $\beta$ :

$$\beta = \int_{-\frac{\pi}{2}}^{\frac{\pi}{2}} \frac{\mathbf{FN}^\theta}{\|\mathbf{FN}^\theta\|} \cdot \mathbf{e}_1 \Psi(\Theta) d\Theta \quad (13)$$

where  $\mathbf{e}_1$  is the unit vector along a privileged direction (e.g. the loading axis). According to this definition,  $\beta$  is comprised in the interval  $[0, 1]$ , where  $\beta = 0$  implies that all fibers are oriented perpendicularly to the privileged direction  $\mathbf{e}_1$  and  $\beta = 1$  implies that all the fibers are parallel to  $\mathbf{e}_1$ . An isotropic fiber distribution is characterized by  $\beta = 2/\pi \approx 0.64$ .

Since Eq. (11) holds for regions of arbitrary size (provided the region is large enough to be representative of the microstructure), the whole fabric can be decomposed into square mesodomains. The mechanical response of mesodomain is given by Eq. (11) and depends of the fiber properties and orientation. This decomposition is a key feature of the model, since it provides the ability to include gradients of field variables through interpolation – as in the standard finite element method – in the analysis of the mechanical deformation of the nonwoven felt while keeping record of the fiber orientation. It is worth noting that the predictions of Cox's model in the case of homogeneous deformation can be recovered in the case of small strains with linear elastic fibers.

### 3.2. Fiber model

The influence of the fiber properties on the mechanical performance of the fabric is introduced in the constitutive model through the nominal stress – stretch  $s_f(\lambda_f)$  function (Eq. 11). Following the experimental results presented above, fibers were assumed to behave as one-dimensional, rate-independent, isotropic, elasto-plastic solids with linear hardening. The total engineering strain can be decomposed into the sum of an elastic (reversible) component,  $e_f^e$  and a plastic (permanent) one,  $e_f^p$ :

$$e_f = e_f^e + e_f^p \quad (14)$$

The elastic strains are related to the fiber stresses through the fiber elastic modulus

$$s_f = E_f e_f = E_f (\lambda_f^e - 1) \quad (15)$$

while plastic deformation is controlled by the yield function  $\Phi$  given by

$$\Phi = s_f - (s_f^y + H_f \bar{e}_f^p) \quad (16)$$

where  $s_f^y$  and  $H_f$  stand, respectively, for the fiber yield strength and the hardening modulus and  $\bar{e}_f^p$  is the accumulated plastic strain, which is computed as

$$\bar{e}_f^p = \int_0^t \dot{e}_f^p dt. \quad (17)$$

The yield function discriminates between elastic and plastic regimes according to

$$\Phi < 0 \Rightarrow \dot{e}_f^p = 0, \quad (18)$$

$$\Phi = 0 \Rightarrow \begin{cases} \dot{e}_f^p = 0 & \text{for neutral loading} \\ \dot{e}_f^p > 0 & \text{for plastic loading} \end{cases} \quad (19)$$

If  $\Phi > 0$ , the fiber abandons the elastic regime. An elastic trial for the stress carried by the fiber at the instant  $t + dt$  is computed as

$$s_f^{t+dt, \text{trial}} = E_f (e_f^t - \bar{e}_f^{p,t}) = s_f^t + E_f \Delta e_f \quad (20)$$

where  $s_f^t$  is the fiber stress at time  $t$  and  $\Delta e_f$  the strain increment corresponding to  $\Delta t$ . In the plastic regime, the elastic trial stress given by Eq. (20) can be explicitly corrected according to (Simó and Hughes, 1998):

$$s_f^{t+dt} = s_f^{t+dt, \text{trial}} \left[ 1 - \frac{(s_f^{t+dt, \text{trial}} - s_f^y - H_f \bar{e}_f^p) E_f}{s_f^{t+dt, \text{trial}} (E_f + H_f)} \right] = s_f^{t+dt, \text{trial}} (1 - P_c) \quad (21)$$

The term  $P_c$  stands for “plastic corrector” and is used merely for the sake of clarity. The equations for the fiber behavior presented above are only valid for tensile stresses because of buckling under very low compressive stresses. Thus,  $s_f = 0$  whenever compressive stresses are applied to the fibers.

### 3.3. Damage

Damage in thermally-consolidated nonwoven polypropylene fabrics is mainly triggered by interfiber bond fracture. The first effect of bond fracture is to reduce the load carried by the fibers crossing at the broken bond but it also changes the connectivity of the network. Thus, further deformation gives rise to a re-arrangement of the fiber network accompanied by extensive fiber rotation, and fibers are eventually re-loaded as they become aligned to the main loading axis. Finally, fiber fracture occurs in the last stages of deformation well beyond the peak-load in the stress–strain curve. It is evident that these mechanisms, involving changes in the topology of the fiber network, cannot be explicitly accounted for in a continuum model like the one presented here and a phenomenological approach was adopted. This approach includes bond fracture through a continuum damage model in the fibers based on the evidence that bond fracture leads to a reduction in the stress carried by the fibers. Nevertheless, the model is implemented in such a way that the load carried by damaged fibers can increase at later stages of deformation to account for fiber reloading once they become aligned to the main loading axis.

The one-dimensional damage model for the fibers is defined by a loading function,  $\ell$ , a damage activation function,  $\Phi_d$ , a damage threshold variable,  $r$  and a damage value,  $d$ . The loading function,  $\ell$ , determines the onset of damage for a certain loading state, and it is expressed as

$$\ell = \frac{s_f}{b} \quad (22)$$

where  $b$  is the interfiber bond strength. The attempts to measure the bond strength were not successful (Ridruejo et al., 2011), but progressive bond fracture during deformation suggested a large variability in bond strength. Thus, it was assumed that  $b$  followed

a Weibull distribution, and the fracture probability of the bond  $p$  was given by the cumulative distribution function:

$$p = 1 - \exp \left[ - \left( \frac{b - b_0}{B} \right)^m \right] \quad (23)$$

where  $b_0$  stands for the lower bound for the bond strength, and  $B$  and  $m$  control the shape of the Weibull distribution. A Weibull distribution of this form was chosen because it is more flexible than other distributions (e.g. a normal distribution). In particular, it allowed to consider a lower threshold for the bond strength, as the experimental observations suggested. Regardless of the statistical distribution, it was assumed that  $b < s_f^y$ , the fiber tensile strength.

The damage activation function,  $\Phi_d (\leq 0)$ , analogous to the yield function in plasticity, establishes the onset of damage and is given by

$$\Phi_d = \ell - r \quad (24)$$

where  $r$ , the damage threshold variable, stores the magnitude of  $\ell$  at which damage increases.  $r = 1$  for intact fibers and increases progressively with damage up to  $\infty$  when the fiber is completely broken.

The evolution of damage follows the Kuhn-Tucker conditions, which establish

$$\Phi_d \leq 0 \quad \text{and} \quad \dot{r} \geq 0 \quad \text{and} \quad \dot{r} \Phi_d = 0 \quad (25)$$

If  $\Phi_d < 0$ , the fiber behavior follows the elasto-plastic model presented in the previous section while damage is activated when  $\Phi_d = 0$  and the rate  $\dot{\ell}$  is to be evaluated. Negative values of  $\dot{\ell}$  correspond to elastic unloading, which takes place without damage progress. If  $\dot{\ell} > 0$ , there is an increase in damage threshold  $\dot{r}$ , which is determined by the consistency condition requiring that  $\Phi_d = 0$  during the whole damage process. Thus:

$$\dot{\Phi}_d = \dot{\ell} - \dot{r} = 0 \Rightarrow \dot{r} = \dot{\ell} \quad (26)$$

and an explicit expression of the damage threshold function  $r$  can be obtained at each instant by the integration along the loading path of the loading function rate  $\ell$ , leading to

$$r = \max \{ 1, \max \{ \ell \} \} \quad (27)$$

which makes the accumulative nature of damage evident.

Finally, an exponential damage law links the damage threshold  $r$  and the damage value  $d$  according to

$$d = 1 - \frac{1}{r} \exp[A(1 - r)] \quad (28)$$

where the parameter  $A$  controls the area under the stress-strain curve, i.e. the energy dissipated during fracture per unit volume of fibers,  $g_f$ . This energy is obtained by integrating the rate of dissipation and the relationship between both magnitudes is given by

$$g_f = \int_0^\infty b \dot{d} dt = \int_1^\infty b \frac{d}{r} dr = \frac{(2 + A)b^2}{2E_f A} \quad (29)$$

In our phenomenological approach,  $g_f$  represents the energy dissipated during fiber deformation and the contributions due to frictional sliding between fibers after bond fracture and to fiber pull-out after fiber fracture. It is obvious that the total amount of energy dissipated by these mechanisms cannot be estimated directly and can only be inferred from the total amount of energy dissipated by the fabric during a tensile test.

The practical implementation of this model is depicted in Fig. 4. If damage is attained during the elastic regime (Fig. 4(a)), the elastic trial stress in the fiber at the time  $t + \Delta t$ ,  $s_f^{trial} (> b)$  is given by Eq. (20). This magnitude is used to compute the new damage threshold  $r^{t+\Delta t}$  and the new damage variable  $d^{t+\Delta t}$  according to Eqs. (26) to (28). The stress in the damaged material,  $s_f^{t+\Delta t}$ , is

obtained as the secant line starting at the origin with a slope given by  $E_f(1 - d^{t+\Delta t})$  (Fig. 4(a)):

$$s_f^{t+\Delta t} = (1 - d^{t+\Delta t}) E_f (e_f^{t+\Delta t}) = (1 - d^{t+\Delta t}) s_f^{t+\Delta t, trial} \quad (30)$$

If damage begins in the plastic regime (Fig. 4(b)), the trial stress at the time  $t + \Delta t$  is obtained as

$$s_f^{trial} = E_f (e_f^{t+\Delta t} - \bar{e}_f^{p,t}) \quad (31)$$

where  $\bar{e}_f^{p,t}$  stands for the accumulated plastic strain at time  $t$ , and the same procedure is used to update the values of the damage threshold and of the damage variable  $d^{t+\Delta t}$ . The stress in the damaged material,  $s_f^{t+\Delta t}$ , is obtained as the line starting at  $\bar{e}_f^{p,t}$  with a slope given by  $E_f(1 - d^{t+\Delta t})$  as (Fig. 4(b))

$$s_f^{t+\Delta t} = (1 - d^{t+\Delta t}) E_f (e_f^{t+\Delta t} - \bar{e}_f^{p,t}) = (1 - d^{t+\Delta t}) s_f^{t+\Delta t, trial} \quad (32)$$

If at a certain time step the fiber is damaged, the accumulated plastic strain is frozen ( $\bar{e}_f^{p,t+\Delta t} = \bar{e}_f^{p,t}$ ). One interesting feature that has to be included in the damage model is that bond fracture may lead to an initial reduction in the load carried by the fibers. Due to changes in the connectivity of the fabric, however, fibers can be re-loaded at later stages as the fabric deforms and fibers are subjected to large rotations. One simple way to include this effect into the continuum framework is to assume that the bond strength  $b$  is not constant but may vary during deformation. Thus, the bond strength is computed at each time increment using a Monte Carlo lottery and the Weibull distribution of Eq. (23). If the bond strength is below the fiber trial stress, the damage model presented above is used to determine the increment of damage and the new stress carried by the fiber. Otherwise, the fiber is reloaded and the elastic trial stress at time  $t + \Delta t$ , is given again by Eq. (20) (Fig. 4(c)). If this elastic trial stress is lower than the current fiber yield stress ( $s_f^{trial} < (s_f^y + H_f \bar{e}_f^{p,t})$ ), it has to be corrected only for the previously accumulated damage  $d^t$  and the stress  $s_f^{t+\Delta t}$  is expressed by

$$s_f^{t+\Delta t} = (1 - d^t) E_f (e_f^{t+\Delta t} - \bar{e}_f^{p,t}) = (1 - d^t) s_f^{t+\Delta t, trial} \quad (33)$$

If  $s_f^{trial} \geq s_f^y + H_f \bar{e}_f^{p,t}$  (Fig. 4(d)), the fiber undergoes plastic deformation during reloading and the plastic correction has to be added, leading to

$$s_f^{t+\Delta t} = (1 - d^t) (1 - P_c) s_f^{t+\Delta t, trial} \quad (34)$$

Some final remarks can be added for a better understanding of the model. Firstly, damage is decoupled of the fiber plastic yielding. Secondly, the Weibull distribution is usually associated to failure analysis within the weakest link model. According to this model, the probability of finding a critical defect leading to the failure depends on the volume. This is not, however, the underlying hypothesis in the damage model described here: the failure of a bond does not imply the failure of the whole mesodomain and the bond strength is not linked to the mesodomain area. Moreover, bonds are subjected to variable levels of stress and the bond strength also changes according to the Montecarlo lottery, so the fibers are loaded and unloaded during deformation. All these facts reduce significantly the sensitivity of damage with respect to the number of Montecarlo draws. Thirdly, the whole model is formulated in total strains, which ensures the consistency of damage growth. Finally, fiber stresses are explicitly obtained by means of corrections from an elastic trial (return mapping algorithm). The absence of additional iterations reduces greatly the computational cost of the model and offsets the time required to perform the angular integration of Eq. (11).

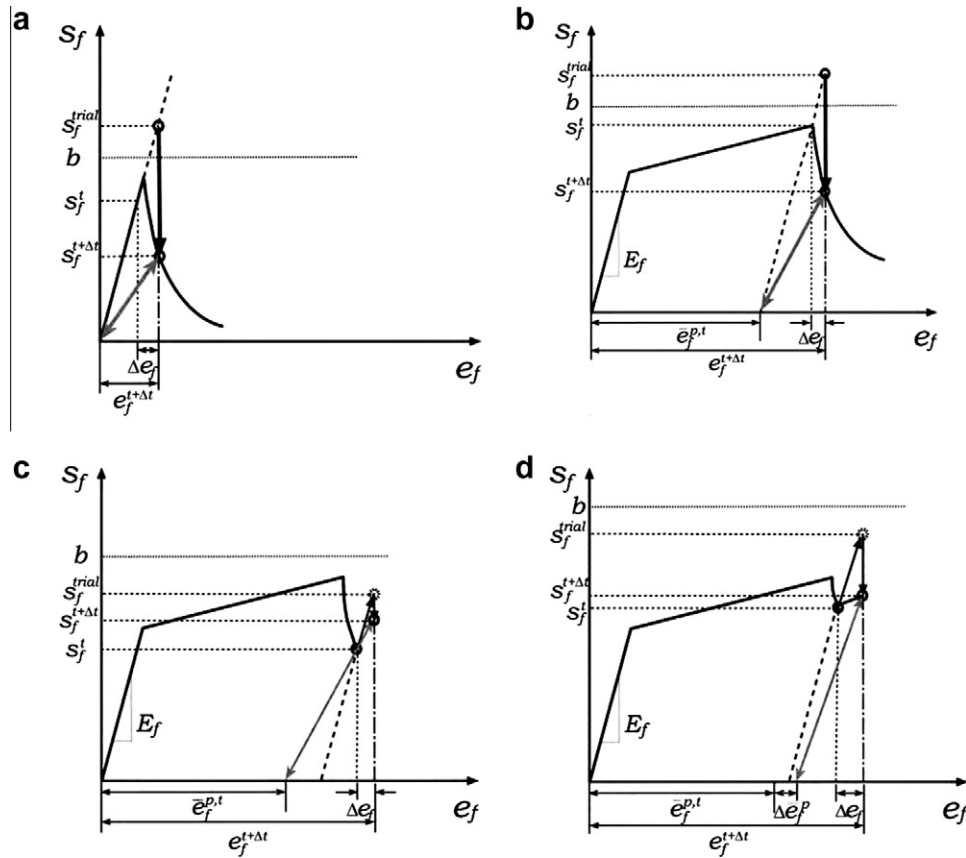


Fig. 4. Damage model. (a) Damage in the elastic regime. (b) Damage in the plastic regime. (c) Reloading in the elastic regime. (d) Reloading in the plastic regime.

#### 4. Numerical implementation

The constitutive model developed in the previous section was implemented as a VUMAT subroutine in Abaqus/explicit. The numerical simulations were carried out under plane stress conditions within the framework of quasi-static deformations and large displacements and rotations with the initial unstressed state taken as reference. The equations of motion for the body were integrated using an explicit central difference integration rule together with the use of diagonal (“lumped”) element mass matrices. More details can be found in Abaqus (2008).

Rectangular specimens of  $200 \times 100 \text{ mm}^2$  were discretized with  $80 \times 40$  CPS4R bilinear plane stress elements, with reduced integration (1 Gauss point per element) and hourglass control. Selected simulations were carried out with finer meshes ( $160 \times 80$  elements) to assess that the results were independent of the element size. It should be noted that the minimum element size ( $1.25 \times 1.25 \text{ mm}^2$ ) was much larger than the average free segment between fiber intersections in the nonwoven and, thus, the mesodomains in the numerical model were large enough to be representative of the microstructure (Isaksson and Hägglund, 2009a,b; Isaksson, 2010).

The boundary conditions of the coupons reproduced those of the tensile tests in Section 2, in which the displacements on the upper and lower boundaries were prescribed in both directions according to

$$\begin{aligned} \dot{\mathbf{u}}(0, y) = 0, \quad \dot{u}_x(W, y) = v, \quad \dot{u}_y(W, y) = 0 \\ \mathbf{T}(x, 0) = \mathbf{T}(x, H) = 0, \quad x \neq 0, \quad x \neq W \end{aligned} \quad (35)$$

where  $\mathbf{T}$  stands for the tractions applied to the specimen boundary and  $v = 20 \text{ mm/s}$  was the applied velocity on the upper boundary of

the cell. This speed was about twenty times higher than the experimental one to reduce computing time. One simulation carried out at  $v = 2 \text{ mm/s}$  led to the same numerical results, demonstrating that the dynamic effects due to the higher strain rate were negligible.

In each time increment, the explicit finite element analysis provides the VUMAT subroutine for each element the corresponding right stretch tensor  $\mathbf{U}$ .<sup>1</sup>

The fiber fabric in each element was assumed to be isotropic in the reference configuration and is made up of 50 sets of fibers whose orientation varies from  $-\pi/2$  to  $\pi/2$ . The fiber stretch for each set is computed as

$$\lambda_f^\theta = \sqrt{\mathbf{CN}^\theta \cdot \mathbf{N}^\theta} = \sqrt{\mathbf{U}^2 \mathbf{N}^\theta \cdot \mathbf{N}^\theta} \quad (37)$$

Once the increment of deformation in each fiber set has been obtained, the bond strength  $b$  (equal for all fiber sets in the element) is computed using a Monte Carlo lottery and Eq. (23). The elastic trial stress is then computed for each fiber set according to Eq. (20) and the development of damage is determined through Eq. (24). If damage increases, the stress carried by the fiber set is given by either Eqs. (30) or (32). Otherwise, the development of plastic deformation is checked using Eqs. (18) and (19). If yielding occurs, the stress carried by the fiber set is computed according to Eq. (34). If not, the stress carried by the fiber set is computed with Eq. (33).

<sup>1</sup> The VUMAT subroutine has a corotational formulation and the constitutive equation is defined in a corotational coordinate system in which the reference system rotates with the material. Thus,  $\mathbf{R} = \mathbf{I}$  in the corotational formulation because the rotations contained in the deformation gradient  $\mathbf{F}$  are cancelled by the rotation of the reference system and

$$\mathbf{F} = \mathbf{R}\mathbf{U} = \mathbf{U} \quad (36)$$

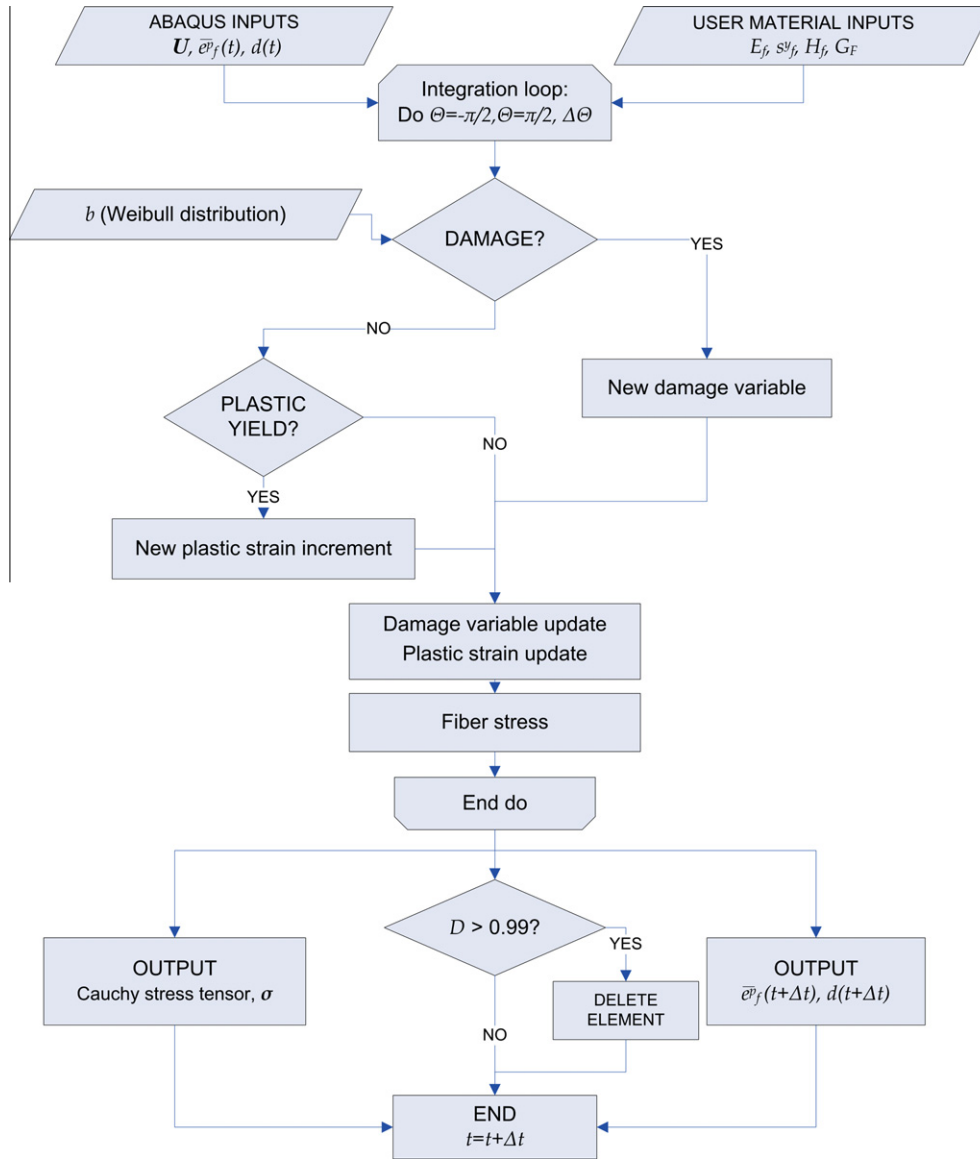


Fig. 5. Flow diagram of the VUMAT subroutine to simulate deformation and fracture of the nonwoven fabric.

The corresponding flow diagram of the VUMAT subroutine is shown in Fig. 5 for the sake of clarity.

Once the stress carried by each fiber set has been determined (and the corresponding values of the accumulated plastic strain, damage threshold and damage have been updated), they are added following Eq. (11) to obtain the constitutive response of the fabric at the element. It should be noted that Eq. (11) was derived using an equivalence with the mechanical power per unit volume in a homogeneous solid. In the particular case of a two-dimensional fabric, the relevant quantities are derived per unit area of the fabric and thus Eq. (11) has to be multiplied by the fabric thickness, which is difficult to measure experimentally because it depends on the applied pressure. Nevertheless, the product of the fiber volume fraction  $f_f$  and the fabric thickness is equal to the ratio  $\rho/\rho_f$  (the areal density of the fabric divided by the density of the polypropylene fibers), which can be easily determined with an analytical balance ( $0.13 \pm 0.02$  mm, Section 2).

In addition to the overall stress carried by the fabric at each element, an average damage variable  $D$  was computed as the average value of the damage variable for all the fiber sets. The elements

with  $D > 0.99$  were removed from the simulations as they were practically broken and carried negligible stresses.

It is well known that the numerical implementation of damage may lead mesh-dependent results because the energy dissipated is a function of the element size. In order to overcome this limitation, the damage evolution law is adjusted using a characteristic element length,  $l_{ch}$ , so that the fracture energy  $G_F$  is independent of the refinement of the mesh (Bazant and Oh, 1983). Mathematically, this condition is introduced as

$$G_F = g_f l_{ch} \quad (38)$$

where  $l_{ch}$  is equal to the square root of the finite element area. Obviously,  $g_f$  depends on the element size and this is introduced through the parameter  $A$ , which is given by

$$A = \frac{2l_{ch}b^2}{2E_f G_F - l_{ch}b^2} \quad (39)$$

where the minimum size of the finite element is limited because the denominator of Eq. (39) has to be positive.



Finally, it should be noted that sudden fracture of the bonds during the simulations introduced local instabilities in the form of high frequency vibrations which impaired convergence. They were eliminated by using bulk viscosity which introduces the pressure term  $P_v$  associated with the volumetric strain rate according to

$$P_v = b_d \rho c_d l_{ch} \dot{\epsilon}_{vol}, \quad (40)$$

where  $b_d$  is a damping coefficient ( $= 0.06$ ),  $c_d$  the dilatational wave speed in the material, and  $\dot{\epsilon}_{vol}$  the volumetric strain rate. This viscous pressure term damps the high frequency oscillations and for this reason it is also known as “truncation frequency damping”. Rather counterintuitively, the presence of damping penalizes the stable time increment to some extent, but it was necessary in order to ensure accurate dynamic modeling.

The convergence and stability of the numerical approach was checked by carrying out simulations with different values for the time step ( $\Delta t$ ), viscous damping ( $b$ ) and loading rate ( $v$ ). The nominal stress–strain curves corresponding to different simulations were equivalent in terms of the maximum load, strain-to-failure and the shape of the post-peak stress–strain curve. In addition, unstable solutions typically display oscillations of increasing amplitude with time in the displacements and the energy balance also changes significantly during the analysis. None of these oscillations were observed. Moreover, all energy components other than strain energy and frictional dissipation – in particular, artificial strain energy – were negligible.

## 5. Results and discussion

The model presented above was used to simulate the mechanical behavior of the smooth and notched specimens of nonwoven polypropylene fabric reported in Section 2. The density and the mechanical properties of the fibers were obtained from tests on individual fibers extracted from the fabric (see Table 1), while the fabric density ( $118 \text{ g/m}^2$ ) was also measured independently. It was not possible, however, to experimentally determine the parameters which control the onset and propagation of damage, i.e.  $b_0$ ,  $B$  and  $m$  together with  $G_F$ , which includes the energy dissipated during fiber fracture as well as by interfiber friction and fiber pull-out after fiber fracture. Although they were chosen to reproduce the experimental results on the smooth specimens (they can be found in Table 2), their values are linked to variables that can be measured independently. For instance,  $b_0$  dictates the stress in the fibers at which damage by interfiber fracture began and its low value leads to the initiation of damage at very low strains, in agreement with the experimental results (Ridruejo et al. (2011)). Moreover,  $b$  is always limited by the fiber strength,  $s_f^u$  and the fracture energy,  $G_F$ , controls the total energy dissipated during the tensile test, which is related to the area under the nominal stress–strain curve.<sup>2</sup> In addition, to check the validity of these parameters, they were used to reproduce the mechanical behavior of the notched samples, where the stress state in front of the notch root is very different to the one found in smooth samples tested in uniaxial tension.

### 5.1. Smooth specimens

The numerical results of the nominal stress (force per unit width) under uniaxial tension are plotted in Fig. 6(a) as a function of the engineering strain for a smooth specimen of  $200 \times 100 \text{ mm}^2$ , together with the corresponding experimental results. The four

**Table 2**

Parameters controlling the onset and propagation of damage in the nonwoven fabric.

$b_0$ (MPa)	$B$ (MPa)	$m$	$G_F$ (kJ/m <sup>2</sup> )
20	360	3.6	550

numerical curves (plotted as thick lines) were obtained using the same set of properties as for the nonwoven fabric. The differences in the mechanical response after the onset of damage were due to the stochastic nature of the model, in which bond strength is computed at each time increment using a Monte Carlo lottery and the Weibull distribution Eq. (23). It should be noted that the differences in the stress–strain curves among nominally identical numerical simulations were similar to those reported experimentally, showing the model’s ability to reproduce the random nature of the nonwoven fabric. The four dashed lines in Fig. 6(b) correspond to other numerical simulations carried out with the same material parameters and boundary conditions but with finite elements whose area was four times smaller. These simulations, generally more costly from a computational viewpoint due to the higher number of elements and to the reduction in the time step, provided equivalent results in terms of maximum load, strain-to-failure and post-peak response, although they presented more scatter concerning the strain at which the load dropped. This demonstrates that the results provided by the numerical model were practically independent of the finite element size.

The features of the numerical curves reproduced very accurately the experimental ones (Fig. 6(a)). The initial linear region was followed by a nonlinear zone due to the homogeneous nucleation of damage throughout the specimen by interbond fracture. This process continued until a maximum in the load carrying capability was achieved (at engineering strains of the order of 30–40%), and it was followed shortly afterwards by the localization of damage. The load was not reduced to zero after the localization of damage and the curves presented a long tail associated with the load transferred by a limited number of fibers oriented parallel to the loading axis. It should be noted that the numerical and experimental curves sometimes showed a serrated shape and the load carried by the fabric increased slightly after a sudden load drop. This phenomenon was caused in the real material by the re-organization of the network topology after the fracture of interfiber bonds and it was phenomenologically introduced in our model by the stochastic variation of the interfiber bond strength  $b$  during deformation.

These mechanisms are in very good agreement with those observed during *in situ* mechanical tests in the scanning electron microscope (Ridruejo et al., 2011) and can be seen in the contour plots of the average damage variable  $D$  (Fig. 7) and fiber orientation index  $\beta$  (Fig. 8) corresponding to four different stages during deformation marked as *a*, *b*, *c* and *d* in Fig. 6(a). Damage developed homogeneously during the initial stages of deformation and was slightly higher at the center and at the four corners. This was due to the stress concentration induced in these regions by the barreling effect and the boundary conditions on both ends of the specimen, respectively (Fig. 7(a)). The onset of inhomogeneous damage occurred near to the maximum load (Fig. 7(b)) and it was found at the upper right corner of the specimen in this case. Nevertheless, the actual localization of damage developed from another corner of the specimen (Fig. 7(c)) and this behavior reflects the stochastic nature of the model implemented. As a result, the numerical simulations presented very similar stress–strain curves up to the maximum load, whereas the after-peak response varied as a function of the actual localization path. This behavior is equivalent to the one reported experimentally and reproduces the scatter arising from the stochastic nature of nonwoven fabrics. Once a predominant localization began, it propagated very rapidly across

<sup>2</sup> The actual value of  $G_F$  was thus selected to fit the post-peak behavior but it is not a direct measure of the energy necessary to create a unit of crack surface because of the features of the stochastic damage model.

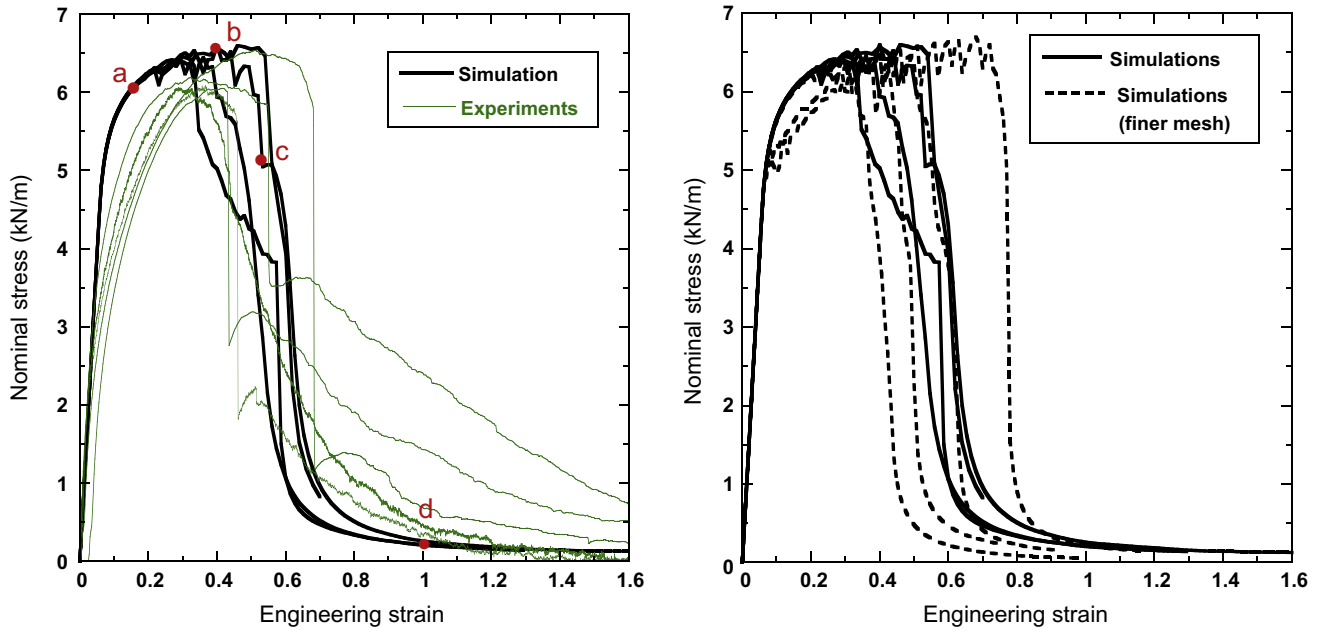


Fig. 6. Nominal stress vs. engineering strain curves for unnotched specimens of  $200 \times 100 \text{ mm}^2$  loaded in uniaxial tension. (a) Thick lines correspond to the numerical simulations obtained with the constitutive model developed in this paper while the thin lines stand for the experimental results in Ridruejo et al. (2011). (b) Solid lines are the same curves as in (a), whereas dashed lines represent simulations in which the area of each finite element was reduced by a factor of 4.

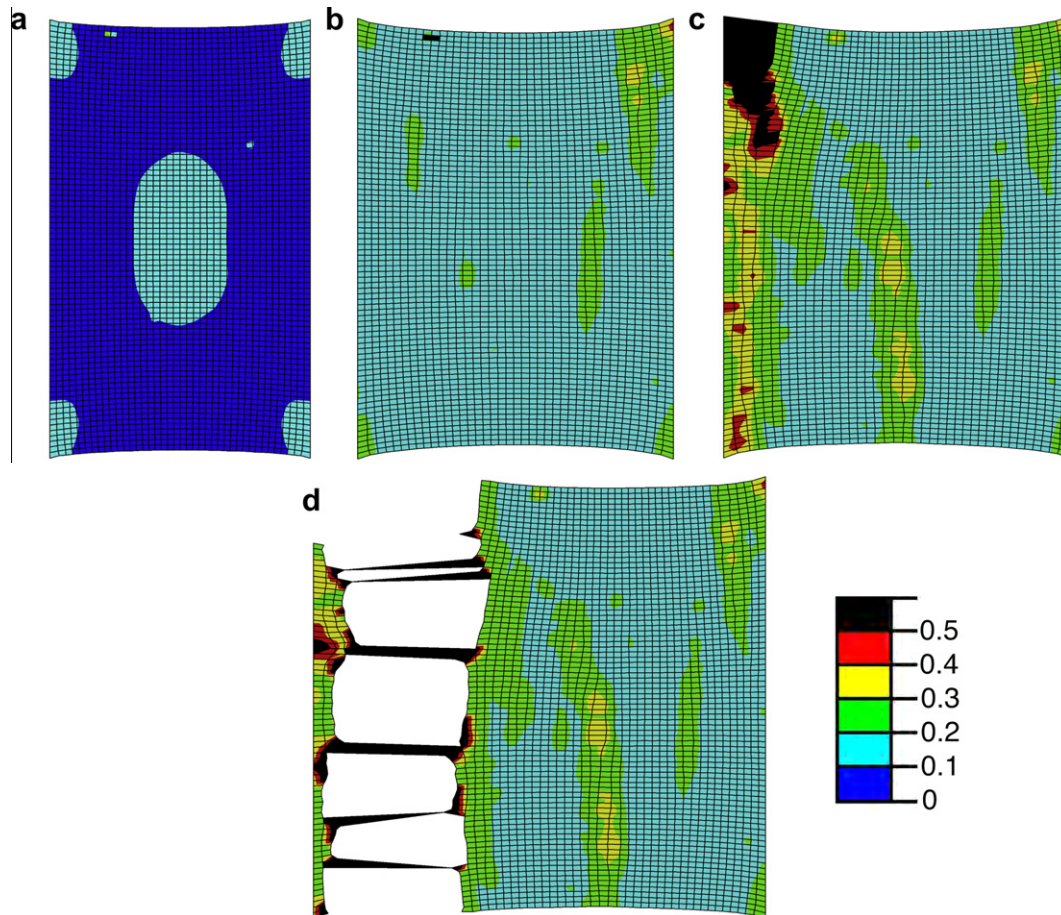
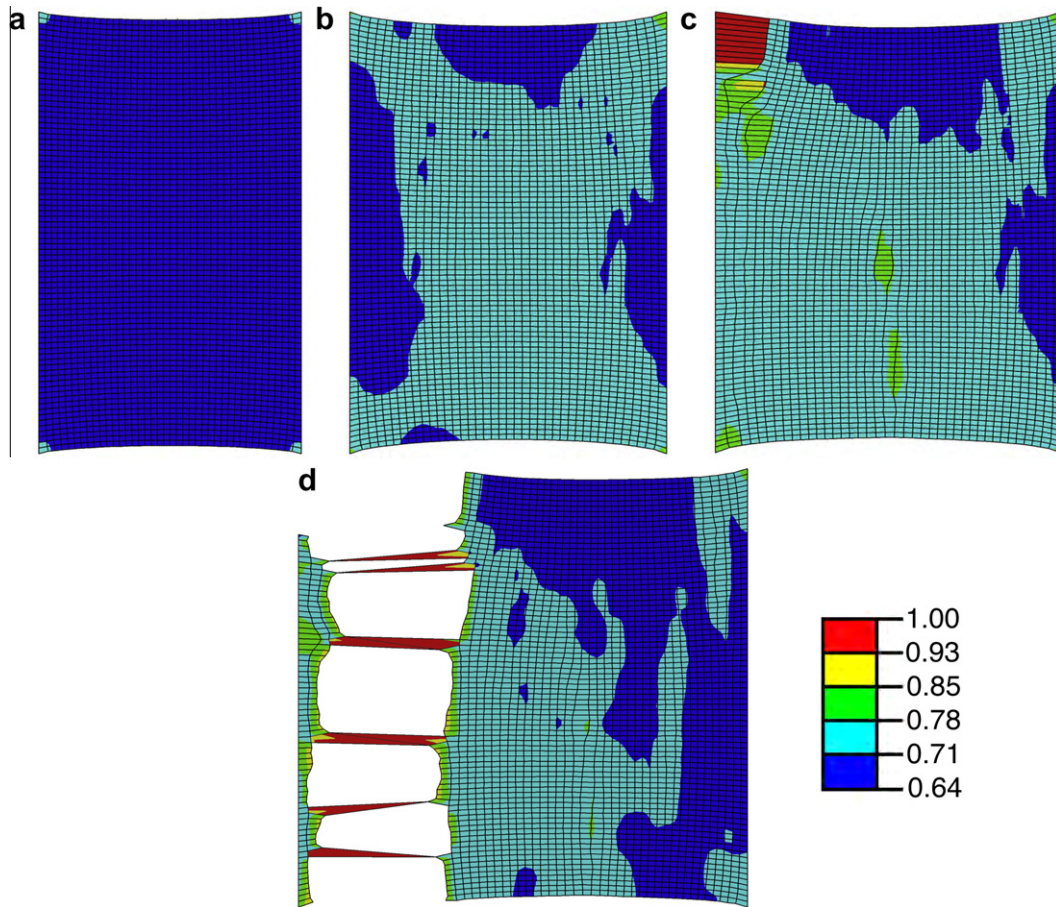
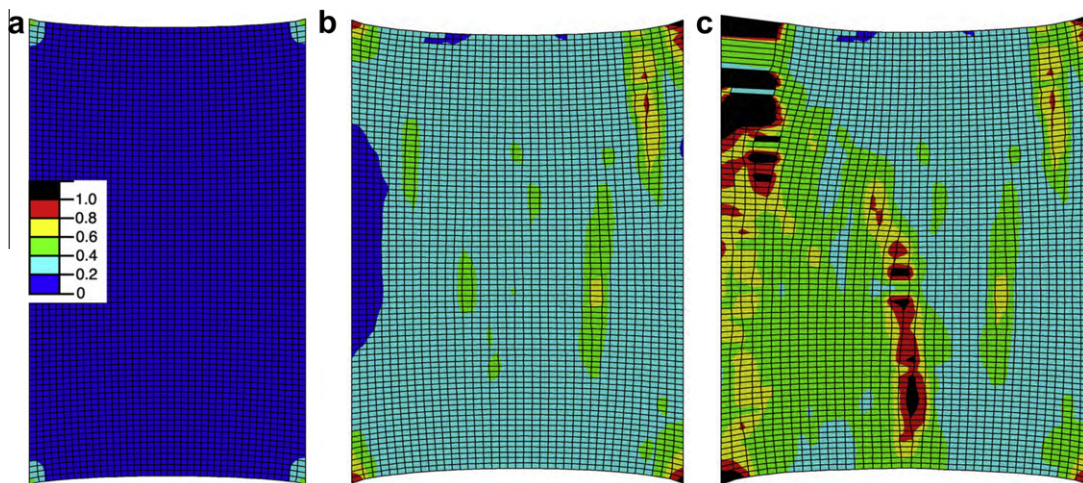


Fig. 7. Contour plot of the average damage variable  $D$  in the smooth specimen subjected to uniaxial tension. (a) Applied strain of 0.16, corresponding to point (a) in Fig. 6(a). (b) Applied strain of 0.40, corresponding to point (b) in Fig. 6(a). (c) Applied strain of 0.53, corresponding to point (c) in Fig. 6(a). (d) Applied strain of 1.0, corresponding to point (d) in Fig. 6(a). Elements with  $D > 0.93$  were deleted for the sake of clarity.



**Fig. 8.** Contour plot of the fiber orientation index  $\beta$  in the smooth specimen subjected to uniaxial tension. (a) Applied strain of 0.16, corresponding to point (a) in Fig. 6(a). (b) Applied strain of 0.40, corresponding to point (b) in Fig. 6(a). (c) Applied strain of 0.53, corresponding to point (c) in Fig. 6(a). (d) Applied strain of 1.0, corresponding to point (d) in Fig. 6(a). Elements with  $D > 0.93$  were deleted for the sake of clarity.



**Fig. 9.** Contour plot of the accumulated plastic strain,  $e_p^p$ , in the fibers oriented parallel to the loading axis in the smooth specimen subjected to uniaxial tension. (a) Applied strain of 0.16, corresponding to point (a) in Fig. 6(a). (b) Applied strain of 0.40, corresponding to point (b) in Fig. 6(a). (c) Applied strain of 0.53, corresponding to point (c) in Fig. 6(a).

the specimen but did not lead, however, to a brittle fracture. The final crack was bridged by a few fabric filaments which led to a long tail in the stress–strain curve.

The model was also able to take into account the progressive reorientation of the fibers upon loading, as measured by parameter  $\beta$  (Fig. 8). Fiber reorientation is minimum during the initial stages

of deformation (Fig. 8(a)) and begins to be noticed near to the maximum load, particularly at the center and the corners of the specimen where the stresses and strains were maxima (Fig. 8(b)). This smooth alignment of the fibers along the loading axis changes abruptly when damage is localized in one corner, leading to a rapid rotation of the fibers in the damaged region (Fig. 8(c)), followed by

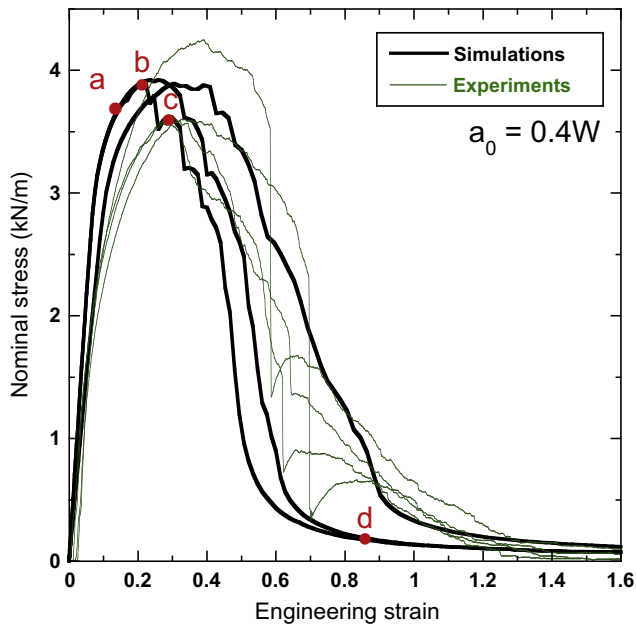


**Fig. 10.** Nominal stress vs. engineering strain curves for the specimen of  $200 \times 100 \text{ mm}^2$  with an initial notch length of 40 mm loaded in uniaxial tension. Thick lines correspond to the numerical simulations obtained with the constitutive model developed in this paper while the thin lines stand for the experimental results in Ridruejo et al. (2011).

fiber fracture and the propagation of a crack across the specimen. The fibers in fabric filaments bridging the final crack were completely aligned in the loading direction (Fig. 8(d)).

Finally, it is also interesting to analyze the evolution of the plastic deformation in the fibers during deformation. The behavior of each element is given by the average of the 50 fiber sets with different orientation and the plastic strain of each fiber set is different. Obviously, the highest stresses are borne by the fiber sets parallel to the loading axis from the beginning, which also undergo the largest plastic strains. The contour plot of the accumulated plastic strain in these fiber sets,  $\bar{\epsilon}_p^p$ , is plotted in Fig. 9 at different stages of deformation. They show that the plastic deformation was initially distributed homogeneously (Fig. 9(a)) and it was concentrated in the corners and at isolated points within the felt at the maximum load (Fig. 9(b)). Upon further loading, plastic strain was localized in two strips perpendicular to the loading axis, one starting from the upper-left corner of the fabric and the other in the center of the specimen, which coincided with the regions of localization of damage. The evolution of the plastic strain in these regions was controlled by the localization of damage, which led to the formation of a dominant crack from the upper-left corner of the felt. As a result, the specimen was unloaded and the plastic strain throughout the specimen was frozen.

## 5.2. Notched specimens

The mechanical behavior of polypropylene nonwoven specimens with the same dimensions and a central notch of 20%, 40% and 60% of the total width was also simulated under uniaxial tension. The material parameters were those used in the analyses of the smooth specimens and three simulations were carried out for each geometry. The nominal stress vs. strain curves of the specimen with an initial notch of 0.4 W are plotted in Fig. 10, together with the corresponding experimental results. The overall agreement between the numerical simulations and the experimental re-

**Table 3**

Average values of the nominal strength (in kN/m) as a function of the initial notch length. The experimental results correspond to a minimum of 4 tests while the numerical ones are the average of 3 simulations.

Notch length	0	0.2 W	0.4 W	0.6 W
Experiments	$6.2 \pm 0.1$	$5.2 \pm 0.2$	$3.7 \pm 0.2$	$2.4 \pm 0.1$
Simulations	$6.32 \pm 0.04$	$4.95 \pm 0.12$	$3.70 \pm 0.04$	$2.60 \pm 0.04$

sults is very good. Besides, the model was able to capture the maximum load-bearing capacity of the felt, the post-peak behavior and the variability in the experimental curves due to the inherent randomness of the material. Similar results were obtained for the samples for initial notches of 0.2 and 0.6 W and they were not plotted for the sake of brevity.

The average values of the nominal strength carried by smooth and notch specimens is shown in Table 3. It is worth noting that both the experimental results and the numerical model predict a notch-insensitive behavior in which the reduction in the fabric strength is proportional to the initial notch length. This behavior has also been reported in nonwoven fabrics made up of brittle fibers (Hägglund and Isaksson, 2006; Ridruejo et al., 2010) and it was attributed to the felt randomness and the limited strain concentration in front of the notch tip induced by the sparse fiber network structure. In the case of the polypropylene fabrics, notch insensitiveness is caused by the large nonlinear deformation capacity of the material, which leads to the complete blunting of the notch tip before failure, as will be shown below.

In addition to the macroscopic behavior, it is also worth analyzing the micromechanisms of damage in front of the notches where the fabric is subjected to a stress state very different from uniaxial tension. The contour plot of the average damage,  $D$ , is shown in Fig. 11. Damage developed very early in front of the notch tips and spread out from there to the lateral surfaces. This process was accompanied by a progressive blunting of the notch tips and by the localization of the strain in front of the notch, and both processes were remarkably similar to the experimental behavior depicted in Fig. 2. The maximum load was dictated by the weakening of the material in front of the notches but was attained well before the elements in front of the notches were completely broken (Fig. 11(b)). Localization of damage was more gradual in the notched specimens, as compared to the smooth ones. Thus, the reduction in the load-bearing capacity of the fabric with strain was also slower and it should be noted that these differences between smooth and notched specimens were also captured by the numerical model. Final fracture occurred by the failure of the fabric in front of the notch after the notch tips were completely blunted (Fig. 11(d)). As in the case of smooth specimens, the final cracks were bridged by a few fabric filaments which led to a long tail in the stress–strain curve, in agreement with the experimental observations (Figs. 2(c) and d).

The evolution of the fiber orientation is shown in Fig. 12 at different stages of deformation. The inhomogeneous stress state induced by the presence of the notch leads to two very different regions. On the one hand, the felt remained fairly isotropic above and below the notch, where the stresses were very low, but the fibers showed a slight trend to align perpendicularly to the loading direction. On the other hand, fibers rapidly rotated and became parallel to the loading axis in front of the notches. Again, this orientation of the fibers perpendicular to the loading axis in front of the notch was corroborated by the experimental observations (Figs. 2(c) and (d)). Finally, the contour plots of the accumulated plastic strain on the fibers showed the expected results, with fiber plasticity concentrated in front of the notches. They are not plotted for the sake of brevity.

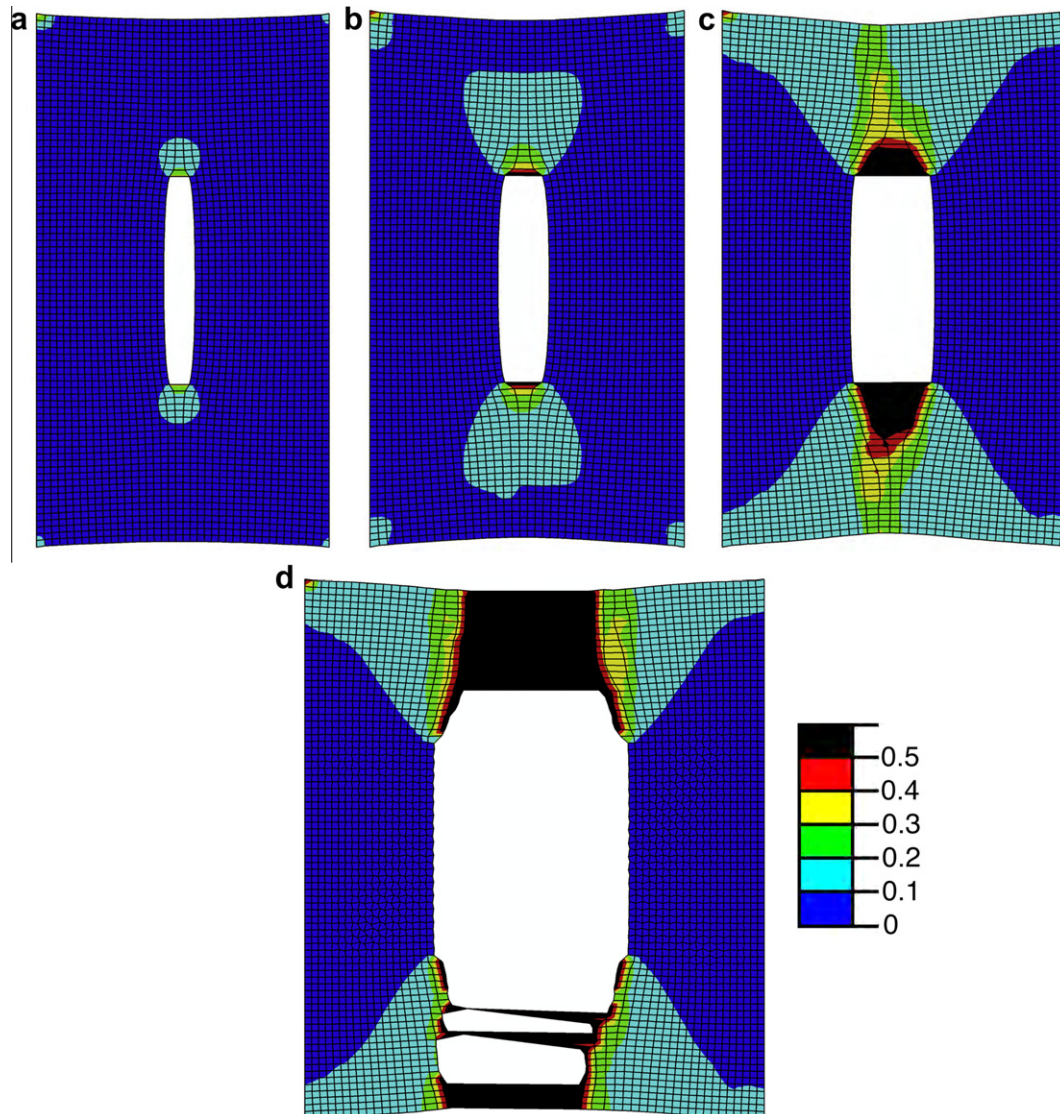


**Fig. 11.** Contour plot of the average damage variable  $D$  in the notched specimen subjected to uniaxial tension. (a) Applied strain of 0.13, corresponding to point (a) in Fig. 10(b). (b) Applied strain of 0.21, corresponding to point (b) in Fig. 10(b). (c) Applied strain of 0.30, corresponding to point (c) in Fig. 10(b). (d) Applied strain of 0.86, corresponding to point (d) in Fig. 10(b). Elements with  $D > 0.93$  were deleted for the sake of clarity.

## 6. Conclusions

A physically-based continuum model was developed to simulate the in-plane mechanical response of nonwoven fabrics. The model provides the constitutive response of the material at the meso-main level and it is thus suitable to be implemented as a material subroutine within the framework of the finite element method. The model is built upon the ensemble of three blocks, namely fabric, fibers and damage to reproduce the actual mechanisms of deformation and fracture experimentally observed. The nonwoven fabric model considers a set of non-interacting straight fibers with arbitrary orientation and uses a rigorous tensorial formulation valid for large deformations and rotations to take into account the evolution of fiber orientation upon loading. The fiber model assumes an elasto-plastic behavior which accurately reproduces the mechanical response of polypropylene fibers. Finally, the effect fiber fracture, fiber pull-out and friction are included in the model by means of a continuum damage model, while the inherent randomness of the

nonwoven microstructure as well as the changes in the fabric topology due to fracture of interfiber bonds are introduced phenomenologically by means of random-variable damage thresholds.

The model was implemented in Abaqus/Explicit as a user material subroutine and was used to simulate the behavior under uniaxial tension of smooth and notched rectangular specimens of a polypropylene nonwoven fabric. The model parameters associated with the fabric and fibers were carefully measured independently, while those related to damage were chosen to reproduce the macroscopic response of the smooth specimens. The model simulations reproduced very accurately the nominal stress–strain curve of smooth and notched samples, as well as the main deformation and fracture micromechanisms, including the rotation of the fibers in different areas of the fabric, the transition from homogeneous deformation to the localization of damage and the final fracture. These results show the potential of this physically-based model to reproduce the complex deformation and fracture micromechanisms of nonwoven fabrics.

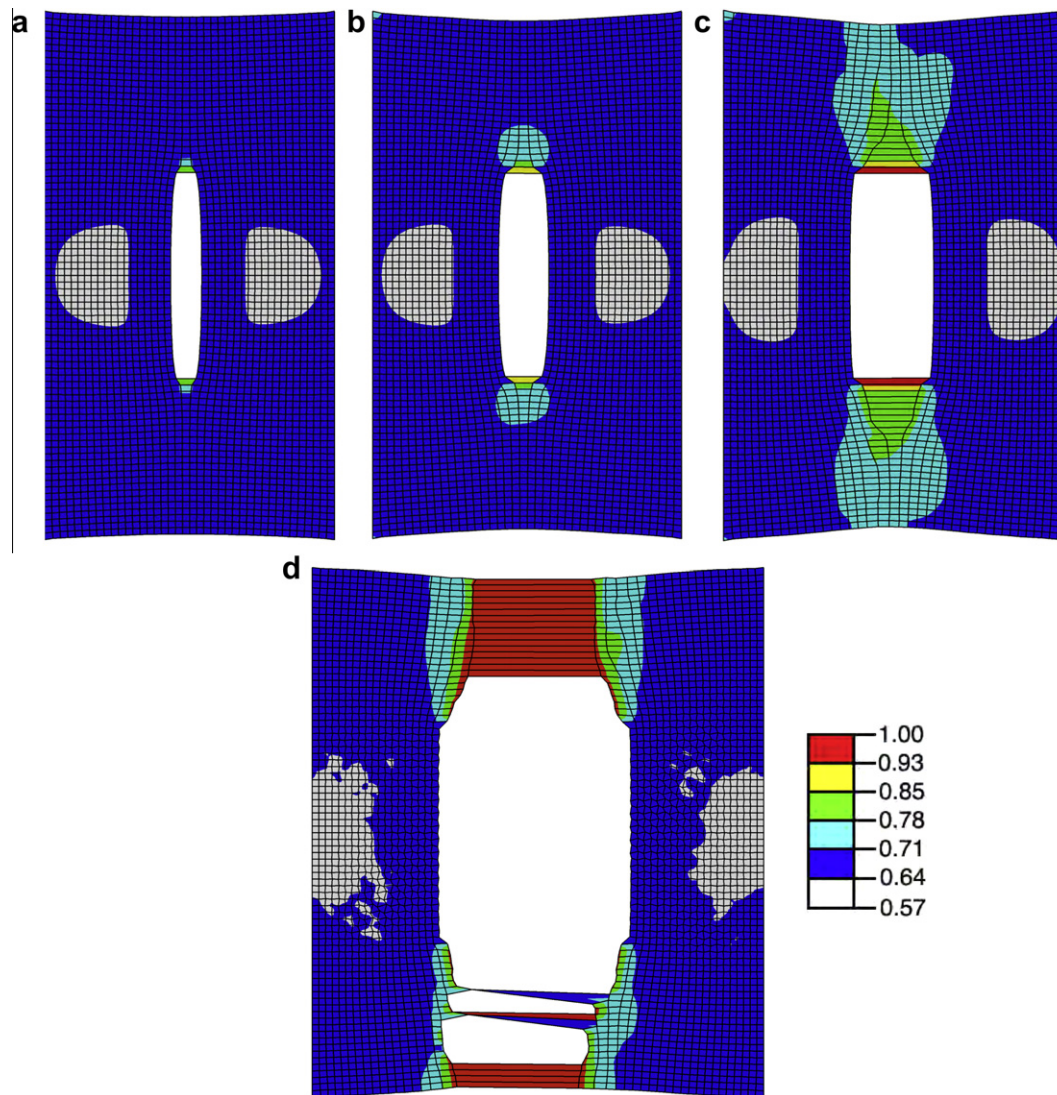


**Fig. 12.** Contour plot of the fiber orientation index  $\beta$  in the notched specimen subjected to uniaxial tension. (a) Applied strain of 0.13, corresponding to point (a) in Fig. 10(b). (b) Applied strain of 0.21, corresponding to point (b) in Fig. 10(b). (c) Applied strain of 0.30, corresponding to point (c) in Fig. 10(b). (d) Applied strain of 0.86, corresponding to point (d) in Fig. 10(b). Elements with  $D > 0.93$  were deleted for the sake of clarity.

## Acknowledgments

This investigation was supported by the Spanish Ministry of Education and Science through Grant MAT2009-14396 and by the Comunidad de Madrid through the Program ESTRUMAT (S2009/MAT-1585).

## References

- Abaqus, 2008. Users' Manual, version 6.7. ABAQUS, Inc.
- Backer, S., Petterson, D., 1960. Some principles of nonwoven fabrics. *Textile Research Journal* 30, 704–711.
- Bais-Singh, S., Goswami, B.C., 1995. Theoretical determination of the mechanical behavior of spun-bonded nonwovens. *Journal of Textile Institute* 86, 271–288.
- Bazant, Z., Oh, B.H., 1983. Crack band theory for fracture of concrete. *Materials and Structures* 16, 155–177.
- Berhan, L., Sastry, A., 2007. Modeling percolation in high-aspect-ratio fiber systems. I. Soft-core versus hard-core models. *Physical Review E* 75, 041120–041128.
- Berhan, L., Yi, Y.B., Sastry, A.M., 2004a. Effect of nanorope waviness on the effective moduli of nanotube sheets. *Journal of Applied Physics* 95, 5027–5034.
- Berhan, L., Yi, Y.B., Sastry, A.M., Munoz, E., Selvidge, M., Baughman, R., 2004b. Mechanical properties of nanotube sheets: alterations in joint morphology and achievable moduli in manufacturable materials. *Journal of Applied Physics* 95, 4335–4345.
- Bischoff, J.E., Arruda, E.M., Grosh, K., 2002. Orthotropic hyperelasticity in terms of an arbitrary molecular chain model. *Journal of Applied Mechanics* 69, 198–201.
- Britton, P.N., Sampson, A.J., Elliott, C.F., Graben, H.W., Gettys, W.E., 1984a. Computer simulation of the mechanical properties of nonwoven fabrics, Part III: fabric failure. *Textile Research Journal* 54, 1–5.
- Britton, P.N., Sampson, A.J., Gettys, W.E., 1983. Computer simulation of the mechanical properties of nonwoven fabrics, Part I: the method. *Textile Research Journal* 53, 363–368.
- Britton, P.N., Sampson, A.J., Gettys, W.E., 1984b. Computer simulation of the mechanical properties of nonwoven fabrics, Part II: bond breaking. *Textile Research Journal* 54, 425–428.
- Carlsson, L.A., Lindstrom, T., 2005. A shear-lag approach to the tensile strength of paper. *Composites Science and Technology* 65, 183–189.
- Cox, H.L., 1952. The elasticity and strength of paper and other fibrous materials. *British Journal of Applied Physics* 3, 72–79.
- Diani, J., Brieu, M., Vacherand, J.M., Rezgui, A., 2004. Directional model for isotropic and anisotropic hyperelastic rubber-like materials. *Mechanics of Materials* 36, 313–321.
- Dzenis, Y., 2004. Spinning continuous fibers for nanotechnology. *Science* 304, 1917–1919.
- Gasser, T.C., Ogden, R.W., Holzapfel, G.A., 2006. Hyperelastic modeling of arterial layers with distributed collagen fiber orientations. *Journal of the Royal Society Interface* 3, 15–35.
- Grindstaff, T.H., Hansen, S.M., 1986. Computer model for predicting point-bonded nonwoven fabric strength, Part I. *Textile Research Journal* 56, 383–388.

- Hägglund, R., Isaksson, P., 2006. Analysis of localized failure in low-basis weight paper. *International Journal of Solids and Structures* 43, 5581–5592.
- Hearle, J.W.S., Stevenson, P.J., 1964. Studies in nonwoven fabrics: Part IV: prediction of tensile properties. *Textile Research Journal* 34, 181–191.
- Isaksson, P., 2010. An implicit stress gradient plasticity model for describing mechanical behavior of planar fiber networks on a macroscopic scale. *Engineering Fracture Mechanics* 77 (8), 1240–1252.
- Isaksson, P., Hägglund, R., 2009a. Strain energy distribution in a crack-tip region in random fiber networks. *International Journal of Fracture* 156, 1–9.
- Isaksson, P., Hägglund, R., 2009b. Structural effects on deformation and fracture of random fiber networks and consequences on continuum models. *International Journal of Solids and Structures* 46 (11–12), 2320–2329.
- Jirsak, O., Lukas, D., 1991. Computer modeling of geotextiles related to mechanical properties evaluated by micromechanics. *Geotextiles and Geomembranes* 10 (2), 115–124.
- Jirsak, O., Lukas, D., Charvat, R., 1993. A two-dimensional model of the mechanical properties of textiles. *Journal of the Textile Institute* 84, 1–15.
- Kallmes, O., Corte, H., 1960. The structure of paper I. The statistical geometry of an ideal two dimensional fiber network. *Tappi Journal* 43, 737–752.
- Kothari, V.K., Patel, P.C., 2001. Theoretical model for predicting creep behavior of nonwoven fabrics. *Indian Journal of Fibre & Textile Research* 26, 273–279.
- Liao, T., Adanur, S., 1999. Computerized failure analysis of nonwoven fabrics based on fiber failure criterion. *Textile Research Journal* 69, 816–824.
- Liao, T., Adanur, S., Drean, J.Y., 1997. Predicting the mechanical properties of nonwoven geotextiles with the finite element method. *Textile Research Journal* 67, 753–760.
- Narter, M.A., Batra, S.K., Buchanan, D.R., 1999. Micromechanics of three-dimensional fiberwebs: constitutive equations. *Proceedings of the Royal Society of London A* 455, 3543–3563.
- Petterson, D.R., 1959. On the Mechanics of Nonwoven Fabrics. Ph.D. Thesis. Massachusetts Institute of Technology.
- Planas, J., Guinea, G.V., Elices, M., 2007. Constitutive model for fiber-reinforced materials with deformable matrices. *Physical Review E* 76, 041903–041909.
- Räisänen, V.I., Alava, M.J., Nieminen, R.M., Niskanen, K.J., 1997. Failure of planar fiber networks. *Journal of Applied Physics* 82 (8), 3747–3753.
- Ridruejo, A., González, C., Llorca, J., 2010. Damage micromechanisms and notch sensitivity of glass-fiber non-woven felts: an experimental and numerical study. *Journal of the Mechanics and Physics of Solids* 58, 1628–1645.
- Ridruejo, A., González, C., Llorca, J., 2011. Micromechanisms of deformation and fracture of polypropylene nonwoven fabrics. *International Journal of Solids and Structures* 48, 153–162.
- Silberstein, M.N., Pai, C.-L., Rutledge, G.C., Boyce, M.C., 2012. Elastic–plastic behavior of non-woven fibrous mats. *Journal of the Mechanics and Physics of Solids* 60 (2), 295–318.
- Simó, J., Hughes, T.J.R., 1998. *Computational Inelasticity*. Springer-Verlag.
- Termonia, Y., 2003. Lattice model for the drape and bending properties of nonwoven fabrics. *Textile Research Journal* 73, 74–78.
- Wu, X.-F., Dzenis, Y.A., 2005. Elasticity of planar fiber networks. *Journal of Applied Physics* 98, 093501.